Anomalous Hall signatures of nonsymmorphic nodal lines in the doped chromium chalcospinel $CuCr_2Se_4$

Subhasis Samanta,[1] Gang Chen,[2,3,*] and Heung-Sik Kim[1,4,†]

[1]*Department of Physics, Kangwon National University, Chuncheon 24341, Korea*

[2]*Department of Physics and Center of Theoretical and Computational Physics, University of Hong Kong, Pokfulam Road, Hong Kong, China*

[3]*State Key Laboratory of Surface Physics and Department of Physics, Fudan University, Shanghai 200433, China*

[4]*Institute for Accelerator Science, Kangwon National University, Chuncheon 24341, Korea*

(Received 15 April 2021; revised 27 October 2021; accepted 7 December 2021; published 15 December 2021)

An emerging phase of matter among the class of topological materials is nodal line semimetals, possessing symmetry-protected one-dimensional gapless lines at (or close to) the Fermi level in k space. When the k dispersion of the nodal line is weak, van Hove singularities generated by the almost flat nodal lines may be prone to instabilities introduced by additional perturbations such as spin-orbit coupling or magnetism. Here, we study the Cr-based ferromagnetic chalcospinel compound $CuCr_2Se_4$ (CCS) via first-principles electronic structure methods and reveal the true origin of its dissipationless anomalous Hall conductivity, which was not well understood previously. We find that CCS hosts nodal lines protected by nonsymmorphic symmetries, located in the vicinity of Fermi level, and that such nodal lines are the origin of the previously observed distinct behavior of the anomalous Hall signature in the presence of electron doping. The splitting of the nodal line via spin-orbit coupling produces a large Berry curvature, which leads to a significant response in anomalous Hall conductivity. Upon electron doping via chemical substitution or gating, or rotation of magnetization via external magnetic field, noticeable change of anomalous Hall behavior occurs, which makes CCS a promising compound for low-energy spintronics applications.

DOI: 10.1103/PhysRevB.104.245126

I. INTRODUCTION

Dissipationless charge or spin transport has been a key concept in condensed matter physics because of realizations of low-power electronic and spintronic devices [1–3] and the long-time preservation of quantum information that it promises [4–7]. The dissipationless transport phenomenon often originates from topology of electronic structures, and it has been a hallmark of various topologically nontrivial states of matter such as quantum anomalous and spin Hall phases [8,9], or topological semimetals such as magnetic Weyl and nodal semimetals [10,11].

Magnetic topological materials, such as topological insulators doped with magnetic ions [12–14] or magnetic nodal semimetals [15–18], are promising candidates to realize dissipationless Hall transport in room-temperature conditions. In terms of practical applications, on the other hand, the vanishing density of states in Weyl or Dirac semimetals at the Fermi level is not favorable for good transport properties. In this regard nodal line semimetals with weak momentum space dispersion, which can host van Hove singularities in the vicinity of the Fermi level, thanks to the one-dimensional line of zero-energy modes with nonvanishing measure in the k space, seem promising in realizing dissipationless Hall transport or engineering various instabilities for practical device applications [19–21].

It was previously reported that a chalcospinel compound, $CuCr_2Se_4$ (CCS) doped with Br, shows dissipationless anomalous Hall transport that is unaffected by the doping-induced disorder [22,23]. Soon after the experimental report it was suggested to be an electronic Berry phase effect [24,25]. However, the origin of the sharp doping-induced sign change in the anomalous Hall conductivity, as observed in both experiment [22] and theory [25], has not been understood well. In light of recent advancements in topological band theory, we revisit the anomalous Hall response of the electron-doped CCS and reveal its origin. We find that the Br-doped CCS in its ferromagnetic state ($T_C \simeq 430$ K) is a half-metallic nodal line semimetal, where the nodal degeneracy at the zone boundary is protected by nonsymmorphic symmetries in the absence of spin-orbit coupling (SOC). Inclusion of Cr and Se SOC slightly splits the nodal degeneracy, generating a substantial sign-changing anomalous Hall response under electron doping because of the nodal-line-induced finite density of states. It is further shown that, thanks to its weak magnetocrystalline anisotropy [26], Br-doped $CuCr_2Se_4$ may show significant field-dependent response of anomalous Hall signatures under external magnetic fields. Therefore it is expected that electron-doped $CuCr_2Se_4$ would become a promising platform for dissipationless charge and spin transport applications.

II. COMPUTATIONAL METHODS

For this study we carried out electronic structure calculations within the local density approximation (LDA) using the Vienna *Ab initio* Simulation Package (VASP) [27]. Detailed

*gangchen@hku.hk

†heungsikim@kangwon.ac.kr

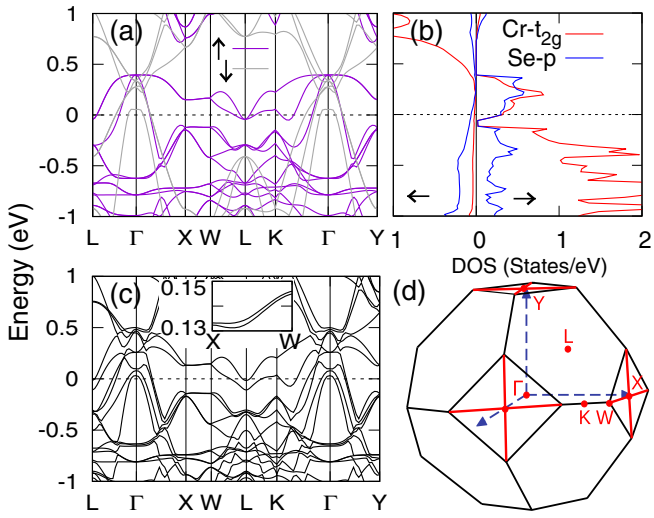

FIG. 1. Spin-polarized band structure and partial density of states (PDOS), obtained using (a), (b) LDA and (c) LDA+SOC with magnetization direction parallel to [111]. PDOS clearly shows van Hove singularities around Fermi level, where nodal lines are seen in the band structure. (d) First Brillouin zone of fcc lattice shows high symmetry points and paths of the nodal lines along X-W with thick red lines.

investigation of spin-orbit coupling and computation of the anomalous Hall conductivity vector was performed using an *ab-initio*-based tight-binding model constructed via the Wannier function [28] method as implemented in the WANNIER90 package [29]. Please refer to the Appendix A for more details.

III. BAND STRUCTURE OF CCS

CCS is a metallic ferrimagnet ($T_C = 430$ K) with a cubic symmetry (space group No. 227), where the ferromagnetic ordering of Cr high-spin moments mostly contributes to the net magnetization [30]. Band structures of CCS with and without spin-orbit coupling are shown in Fig. 1, where Cr-t_{2g}- and Se-p-like hole characters can be clearly seen in the metallic bands close to the Fermi level. Cu states are most located about 2 eV below the Fermi level and weakly contribute to the metallic states. Note that charge configurations of Cu and Cr are not exactly Cu^{+1} and Cr^{3+}, respectively, because of negative charge transfer from Se^{2+} ions to Cr and Cu sites yielding the metallic behavior.

A salient feature of the CCS band structure is the presence of nearly flat twofold-degenerate bands in the majority spin channel [Fig. 1(a)], located close to the Fermi level (within the energy window $|E - E_F| \leqslant 0.15$ eV) on the X-W lines in the absence of spin-orbit coupling. These flat nodal lines induce van Hove singularities around ± 0.15 eV, as shown in the density of states plot [right panel in Fig. 1(a)], while the dispersive minority spin channel almost does not contribute to the states close to the Fermi level [see Fig. 1(b)]. These line degeneracies, namely the so-called Weyl nodal line features [31], are protected by two nonsymmorphic and perpendicular d-glide planes that intersect on every X-W line. Anticommutation relations between the two intersecting glide operations on the X-W lines enforce twofold degeneracy, which can be lifted with the loss of the glide symmetries via lattice distortions or spin-orbit coupling plus symmetry-breaking magnetism.

Indeed, Fig. 1(c) shows the band structure of CCS with including SOC and net magnetization parallel to the [111] direction. A small but finite splitting of the nodal lines on the X-W line is visible. The splitting persists when the magnetization direction is along the [001] axis because of the loss of the glide plane. The orbital-projected density of states close to the nodal lines shows an almost equal mixture of Cr t_{2g} and Se p states [see right panels of Fig. 1(b)], so the splitting of the nodal lines can be attributed to the SOC of Cr d and Se p orbitals.

Recently it has been shown that splitting of nodal lines via SOC results in large intrinsic anomalous Hall or spin Hall signature and topological phases [18,20,32–36]. Thanks to the flat dispersion of the nodal line bands and the resulting finite density of states close to the Fermi level, SOC-induced anomalous Hall signatures in CCS should be significant. Furthermore, small SOC-induced splitting of the nodal lines in CCS may result in a sharp change of anomalous Hall character under charge doping as reported previously [22,23].

IV. WANNIERIZED EFFECTIVE MODEL AND SOC

In order to investigate the role of SOC in anomalous Hall responses, we constructed a tight-binding (TB) Hamiltonian via the Wannier orbital method [28,37,38]. Our Wannierized TB model incorporates 12 Cr-t_{2g}-like and 24 Se-p-like orbitals and faithfully represents nodal lines and other band features of the majority spin channel close to the Fermi level (see Appendix A 2 and Fig. 7 for more details). Note that the contribution of the minority spin channel to the Hall conductivity should be marginal at most because of its negligibly small density of states [see Fig. 1(b)].

In the majority spin channel, where the spin degree of freedom is frozen because of magnetic ordering, SOC behaves as an effective Zeeman field in the orbital sector; $\hat{H}_{SO} \to \hat{\mathcal{P}}_{\mathbf{n}}^{\dagger} \hat{H}_{SO} \hat{\mathcal{P}}_{\mathbf{n}} \simeq \frac{\hbar}{2} \sum_{\alpha} \lambda_{\alpha} \hat{L}_{\mathbf{n}}^{\alpha}$, where α is the index for Cr and Se sites, $\hat{H}_{SO} \equiv \sum_{\alpha} \lambda_{\alpha} \hat{\mathbf{L}}^{\alpha} \cdot \hat{\mathbf{S}}^{\alpha}$ is original atomic SOC, $\mathbf{n}$ is the magnetization direction, and $\hat{\mathcal{P}}_{\mathbf{n}} \equiv \sum_{\alpha} |{\uparrow_{\mathbf{n}}}\rangle_{\alpha} \langle{\uparrow_{\mathbf{n}}}|_{\alpha}$ is a projection operator onto the majority spin channel along $\mathbf{n}$. Hence, SOC on top of nonzero magnetization along $\mathbf{n}$ splits degeneracy between nonzero L_n states, which consist of nodal gapless lines at zone boundaries.

V. ANOMALOUS HALL CONDUCTIVITY

To investigate anomalous Hall responses with respect to net magnetization direction in CCS, we employed the Fukui-Hatsugai-Suzuki method to compute the Berry curvature vector $\boldsymbol{\Omega}(\mathbf{k}) \equiv (\Omega_{yz}, \Omega_{xz}, \Omega_{xy})(\mathbf{k})$ and anomalous Hall conductivity (AHC) in a $96 \times 96 \times 96$ discretized k space [39]. Two magnetization directions, [001] and [111] with respect to the cubic axes, were considered. Both Cr ($\lambda_{Cr} = 0.02$ eV) and Se ($\lambda_{Se} = 0.05$ eV) SOC were included, where values of λ_{Cr} and λ_{Se} were chosen to best fit the energy splitting of two bands close to the Fermi level at the L point. Note that the Berry curvature vector $\boldsymbol{\Omega}(\mathbf{k})$ becomes identically zero at all k points in the absence of SOC because of coexistence of the complex conjugation (i.e., product of

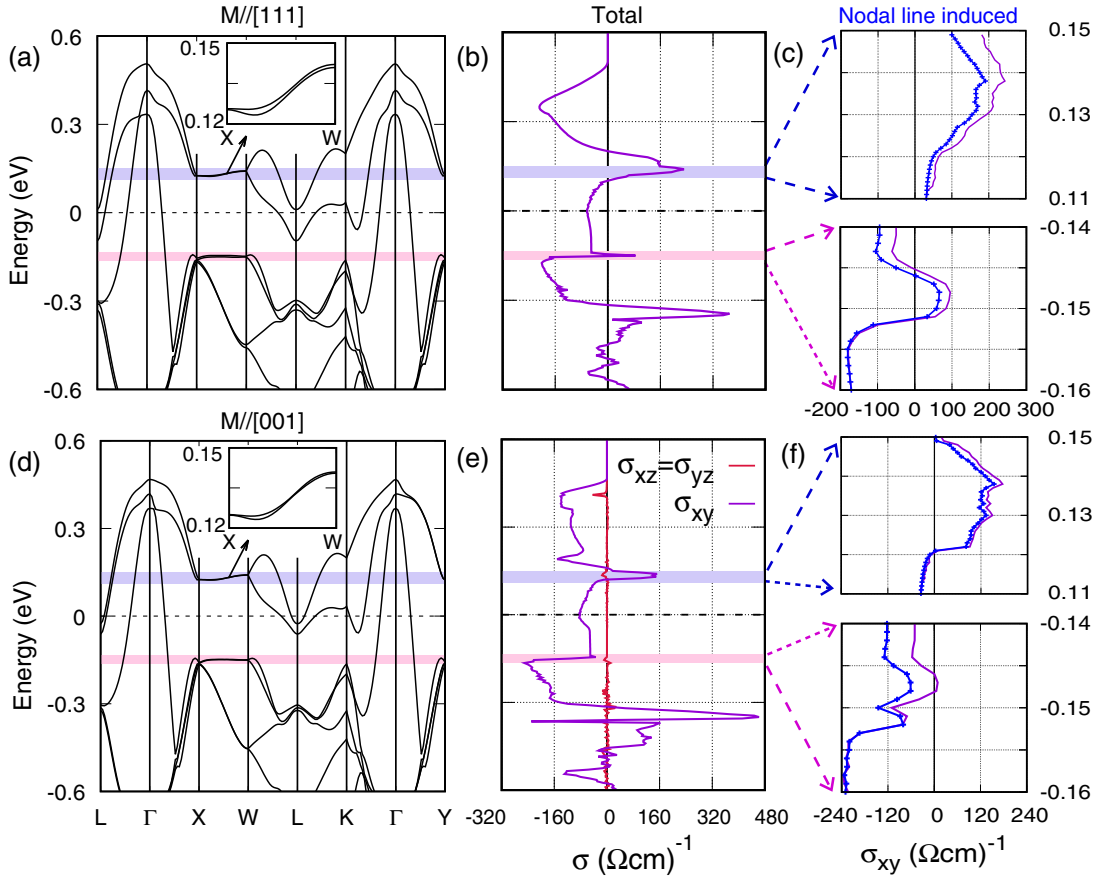

FIG. 2. (a) Band structure in the majority spin channel, obtained from TB Wannier model with magnetization pointed along [111]. Inset shows the splitting of upper nodal line in the enlarged energy window. (b) Three components of total anomalous Hall conductivities are depicted in violet (σ_{xy}) and red ($\sigma_{yz,xz}$) colors. A steep increase in Hall conductivity is observed close to the nodal lines. For $\mathbf{M}//[111]$, all three components are identical. (c) AHC induced by upper (top) and lower (bottom) nodal lines (blue dotted line). (d)–(f) Band structure, total AHC, and nodal lines induced AHC, respectively with $\mathbf{M}//[001]$. The noisy features of $\sigma_{yz,xz}$ in the bottom of panel (e) come from numerical noises that vanish in the limit of infinitely dense k grid.

time-reversal and global spin rotation operations) and inversion symmetries.

Figure 2 shows the effect of spin-orbit coupling on the Wannier TB band structure with different magnetization directions and the resulting anomalous Hall responses. Here, the inclusion of SOC unlocks two conditions necessary for finite anomalous Hall responses; first, as mentioned above, SOC splits nodal line degeneracies by coupling magnetization and band structure so that glide symmetries are lost except ones perpendicular to the magnetization direction. Second, because the global spin rotation symmetry is lost due to SOC, the complex conjugation symmetry which enforces $\mathbf{\Omega}(-\mathbf{k}) = -\mathbf{\Omega}(\mathbf{k})$ is gone. Hence, a finite anomalous Hall response that does not vanish under the k summation emerges from the splitting of the nodal lines via SOC.

The band structures with SOC reveal several important features of the nodal lines. The doubly degenerate nodal lines, which were protected by the nonsymmorphic symmetries in the absence of SOC, are now split via spin-orbit coupling. The insets of Figs. 2(a) and 2(d) show SOC-induced splitting of the upper nodal line. The SOC-induced splitting energy is marginal, of the order of a few meV. The splitting is dependent on the magnetization direction. In the case of [111], nodal line splitting is more pronounced than in the [001] case. The nodal lines also split at the X point, but the magnitude is negligibly small. The direction-dependent splitting is more visible for bands close to E_F at the high symmetry point L.

Anomalous Hall conductivities $\boldsymbol{\sigma}(\mu)$ as a function of chemical potential μ are shown in Figs. 2(b) and 2(e) alongside band plots, where changes in $\boldsymbol{\sigma}(\mu)$ introduced by the presence of SOC and tilting of the magnetization direction from [111] to [001] are shown. Note that anomalous Hall vectors behave in the same way as magnetic moments under symmetry operations, and fourfold and threefold rotation symmetries remain unbroken in the cases of $\mathbf{M}//[001]$ and [111], respectively. Therefore, components of anomalous Hall vectors that are perpendicular to the magnetization cancel out, and only components parallel to the magnetization directions (σ_{xy} when $\mathbf{M}//[001]$, and $\sigma_{xy} = \sigma_{xz} = \sigma_{yz}$ when $\mathbf{M}//[111]$) survive, as shown in Fig. 2. In both cases of $\mathbf{M}//[001]$ and [111], a steep change in Hall conductivity is observed close to the nodal line. Comparing the total AHC for the upper nodal line between [111] and [001], we find that the former is roughly 80 $(\Omega\,\mathrm{cm})^{-1}$ higher in magnitude than the latter one.

From Fig. 2, it is evident that the large enhancement in total AHC occurs close to the nodal lines in the electron-doped region. To see the role of nodal lines, and also to quantify its contribution to total AHC, we have extracted the nodal-line-induced contribution to the AHC. Figures 2(c) and 2(f) show upper- and lower-nodal-line-induced AHC (blue dotted lines) and total AHC (solid violet lines) for the σ_{xy} component with two magnetization directions. Note that we obtained the nodal-line-induced AHC via sampling k points inside thin slabs enclosing the side surfaces of the Brillouin zone that contain the X-W points (slab thickness being 10% of the reciprocal vectors). The result suggests that most of the contribution to total AHC comes from the nodal lines. This confirms that the previously observed large anomalous Hall current in CCS [22] in the presence of Br doping actually stems from the splitting of the nodal line via spin-orbit coupling.

Furthermore, we plot nodal-line-induced Berry curvature in k space. Figure 3(a) shows isosurfaces of magnitudes of energy-integrated magnitudes of Berry curvature vectors, namely, $|\int_{\mu_1}^{\mu_2} d\mu\, \mathbf{\Omega}(\mathbf{k}, \mu)|$, where $\{\mu_1, \mu_2\}$ is set to be $\{0.11, 0.15\}$ and $\{-0.16, -0.14\}$ eV to enclose the nodal lines above and below the Fermi level, respectively. We also considered both the M//[111] and [001] cases. From Fig. 3(a) it can be seen that distribution of the Berry curvature is concentrated on the line connecting the X and W points, so that the sign-changing AHC originates from the splitting of the nodal lines via SOC.

In addition, in Fig. 3(b) we plotted the Berry curvature $\Omega_{xy}(\mathbf{k})$ on one square face of the first Brillouin zone containing X and W points when the magnetization is along the [111] direction [i.e., $\Omega_{xy}(\mathbf{k}) = \Omega_{xz}(\mathbf{k}) = \Omega_{yz}(\mathbf{k})$] with $\mu = 0.125$ eV. Figure 3(b) confirms that the Berry curvature is concentrated on the X-W nodal lines, as shown in Fig. 3(a) and consistent with a previous theoretical finding [25]. It is noted that, with the presence of SOC, the loss of time-reversal symmetry causes an imbalance of Berry curvature at $\mathbf{k}$ and $-\mathbf{k}$ points with respect to the X point and the resulting nonzero net anomalous Hall conductivity.

Figure 4 shows computed $\sigma_{xy}(x)$ as a function of electron doping per formula unit x when $\mathbf{M}$//[111]. Previous experimental Hall conductivity [22] for a few selective doping concentrations is also displayed in the figure for comparison. The Hall response is maximum when doping concentration is close to 0.1, where the doping-induced chemical potential crosses the center of the X-W nodal line dispersion. The sign change behavior is captured around $x = 0.25$. The origin of experimental σ_{xy} close to $x = 1$ should be more complicated due to effects from minority spin bands or impurity scattering, whose contributions are absent in our Wannierized model.

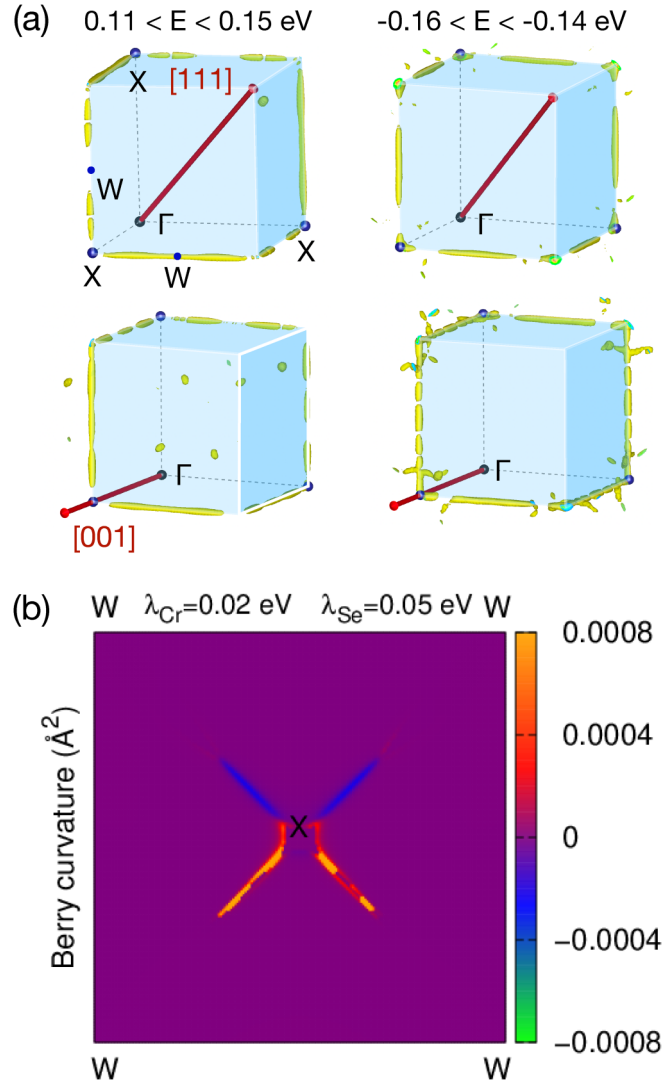

FIG. 3. (a) Isosurfaces of magnitudes of energy-integrated Berry curvature vectors, $|\int_{\mu_1}^{\mu_2} d\mu\, \mathbf{\Omega}(\mathbf{k}, \mu)|$, where the energy range of the integration $\{\mu_1, \mu_2\}$ is chosen to fully include nodal-line-induced Berry curvatures. Left and right panels present results with $\{\mu_1, \mu_2\} = \{0.11, 0.15\}$ and $\{-0.16, -0.14\}$, each of them depicted as violet and pink shades in Fig. 2, respectively. Red arrows represent the direction of the magnetization. (b) $\Omega_{xy}(\mathbf{k}, \mu)$ on the side Brillouin zone surface containing the X-W lines [depicted as blue-shaded planes in (a)], where $\mu = 0.125$ eV and $\mathbf{M}$//[111].

VI. ROLE OF λ_{Cr} ON BAND STRUCTURE AND ANOMALOUS HALL CONDUCTIVITY

In Fig. 2, the electronic band structure and anomalous Hall conductivity are shown in the presence of both Cr and Se SOC. In order to see the role of λ_{Cr}, we computed band structures and AHC with only including λ_{Se} (no λ_{Cr}), as presented in Fig. 5. A close-up view of the upper nodal line splittings without λ_{Cr} [insets in Figs. 5(a), 5(c)], in comparison to the result with both λ_{Cr} and λ_{Se} included [insets in Figs. 2(a), 2(d)], reveals that for $\mathbf{M}$//[111], inclusion of λ_{Cr} narrows the gap, while there is almost no change of splitting for $\mathbf{M}$//[001]. However, the effect of λ_{Cr} is clearly reflected in the anomalous Hall response as shown in Figs. 5(b) and 5(d). Since nodal line bands consist of hybridized Cr-t_{2g}–Se-p states, without λ_{Cr} the AHC, which had spiky features at the upper nodal lines, is sharply peaked with inclusion of λ_{Cr} (Fig. 2). Together this result suggests that both magnetization direction and SOC on both Cr and Se are equally important in order to explain the sign-changing anomalous Hall response close to the nodal lines in the electron-doped regime of this compound.

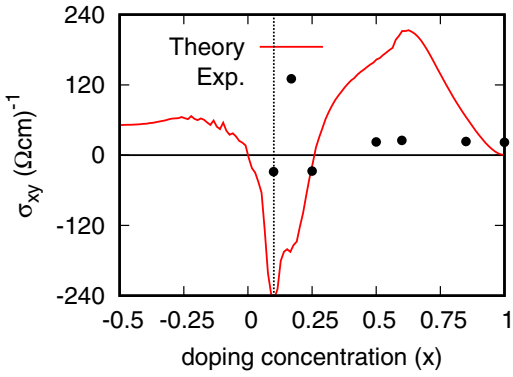

FIG. 4. Hall conductivity in the presence of nonzero λ_{Cr} and λ_{Se} when M//[111], plotted as a function of doping. For comparison, experimental Hall conductivity (measured at 5 K), adopted from Ref. [22] for a few doping concentrations ($x = 0.1$, 0.25, 0.5, 0.6, 0.85, 1), are shown with filled circles. Vertical dotted line located around $x = 0.1$ marks the position of center of the X-W nodal line dispersion in our calculation [see Fig. 2(b)].

VII. POTENTIAL ON-SITE CORRELATION EFFECTS

In the splitting of nodal lines and the resulting anomalous Hall effect in $CuCr_2Se_4$, the role of Cr atomic Hund's coupling that gives rise to $S = 3/2$ Cr local moments is crucial. After the Cr-moment-based ferromagnetism occurs, the electronic structure calculation results within density functional theory provide a good agreement with experimental observations. However, it always remains to be a valid question whether other parts of Coulomb correlations, such as on-site repulsion, might play a significant role even in metallic systems. To better understand the effect of on-site Coulomb repulsion at Cr sites, we have performed DFT+U [40] and DFT+DMFT (dynamical mean-field theory) [41,42] calculations.

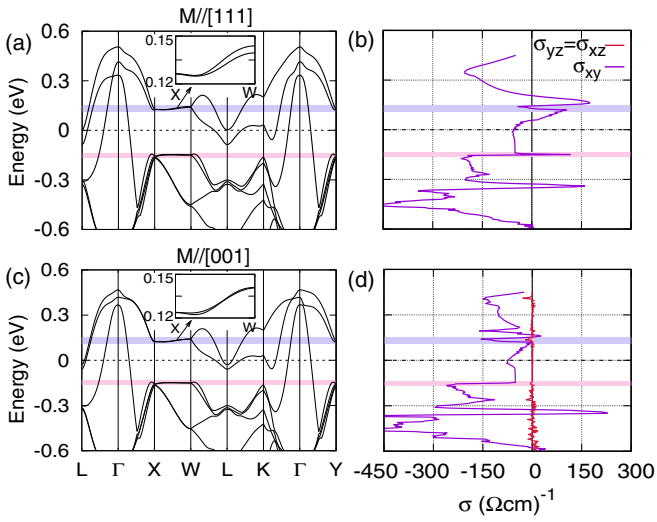

FIG. 5. (a), (b) Band structure and total anomalous Hall conductivity, calculated for the majority spin channel with **M**//[111] in the presence of λ_{Se}. (c), (d) Same band structure and total AHC are now shown for **M**//[001]. The shaded regions highlight the nodal lines.

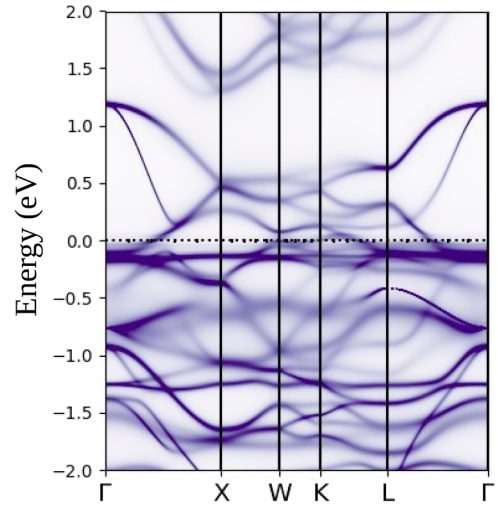

FIG. 6. A majority spin spectral function $A(k, \omega)$ obtained from our DMFT calculation.

Figure 6 shows a momentum-dependent spectral function $A(k, \omega)$ of the majority spin channel of CCS from our DMFT calculation. We notice that majority spin bands are pushed above the Fermi level so that nodal lines lie above the Fermi level within the energy window of 0.4–0.5 eV. $A(k, \omega)$ shows metallic bands (i.e., clear bandlike features without much broadening of spectra) even with the presence of on-site correlations. The top nodal line, located about 0.6 eV above the Fermi level, remains almost dispersionless, while the other two nodal lines located about $0 \sim 0.5$ eV above the Fermi level are slightly dispersive along the X-W line. This shows the robustness of nodal line features and electron-doped anomalous Hall signatures under dynamical electron correlation effects, suggesting that our finding of nodal-line-induced anomalous Hall signatures in doped $CuCr_2Se_4$ is relevant to previous experimental findings [22,23].

Interestingly, it is found that DFT+U tends to drive this system away from the half-metallic regime, which is inconsistent with experimental observations of strong half metallicity in this compound [30,43] (see Fig. 10 and Appendix B for further details), while the the nearly flat nodal line features remain stable under the effect of dynamic on-site correlations within DFT+DMFT. This origin of this contrasting behavior between DFT+U and DFT+DMFT is unclear at this moment.

VIII. DISCUSSION AND SUMMARY

The change in magnitude of anomalous Hall conductivity between [001] and [111] near nodal lines reveals that the direction of magnetization also plays a key role in tuning the Hall response. In addition, according to our density functional theory calculations, the energy difference between the [001] and [111] FM magnetization directions is found to be very small, 0.098 meV per formula unit (f.u.). This is mostly due to the relatively weak spin-orbit coupling constants at Cr atoms and the basal cubic symmetry. Earlier experimental studies show first and second order anisotropy constants to be of the same order ($K_1 = 0.084$ and $K_2 = 0.011$ meV/f.u.), consistent with our finding [26]. Hence, a not-too-strong external

magnetic field of less than a tesla may easily switch the magnetization direction and induce a huge anomalous Hall response in this system.

In conclusion, we explain the origin of the large anomalous Hall behavior in doped $CuCr_2Se_4$. Our analysis reveals that the doubly degenerate nodal line along X-W in the vicinity of the Fermi level is responsible for a large Hall signature. In the presence of spin-orbit coupling, splitting of nodal lines produces a nonzero Berry curvature along X-W, resulting in a large change in the anomalous Hall response. In addition, weak magnetocrystalline anisotropy in $CuCr_2Se_4$ is favorable because it facilitates the switching of the magnetization direction and the resulting anomalous Hall conductivity with the application of an external magnetic field. With these, doped $CuCr_2Se_4$ becomes a promising candidate for studying magnetic topological semimetals and realizing low-power dissipationless spintronics applications.

ACKNOWLEDGMENTS

We thank Bohm-Jung Yang for fruitful discussions. S.S. was funded by the Korea Research Fellow (KRF) Program of the National Research Foundation of Korea (Grant No. 2019H1D3A1A01102984), and also thanks the National Supercomputing Center of Korea for providing computational resources including technical assistance (Grant No. KSC-2020-CRE-0156). H.S.K. acknowledges the support of the National Research Foundation of Korea (Basic Science Research Program, Grant No. 2020R1C1C1005900). G.C. was supported by the Ministry of Science and Technology of China with Grants No. 2018YFE0103200, No. 2016YFA0300500, and No. 2016YFA0301001, by the Shanghai Municipal Science and Technology Major Project with Grant No. 2019SHZDZX01, and by the Research Grants Council of Hong Kong with General Research Fund with Grant No. 17303819.

APPENDIX A: COMPUTATIONAL DETAILS

1. Density functional theory

Density functional theory (DFT) calculations are performed within the projector-augmented-wave (PAW) based Vienna *Ab initio* Simulation Package (VASP) [27]. For all self-consistent total energy calculations and structural relaxations, the plane-wave energy cutoff is set to be 550 eV. A Γ-centered $10 \times 10 \times 10$ k grid is used for sampling the Brillouin zone. To account for electron correlations, the Ceperley-Alder local density approximation (LDA) is adopted [44]. An additional effective Hubbard-type on-site Coulomb repulsion U ($U_{\text{eff}} = 2$, 4 eV) is applied to the d orbitals of Cu and Cr via a simplified rotationally invariant DFT+U approach [40]. For relaxation of electronic degrees of freedom, the energy convergence criteria is chosen to be 10^{-8} eV. Furthermore, spin-orbit coupling is included in the calculations to investigate the topological features of the band structure. The direction of magnetization is assumed to be parallel to the [001] and [111] directions in the conventional cubic unit cell.

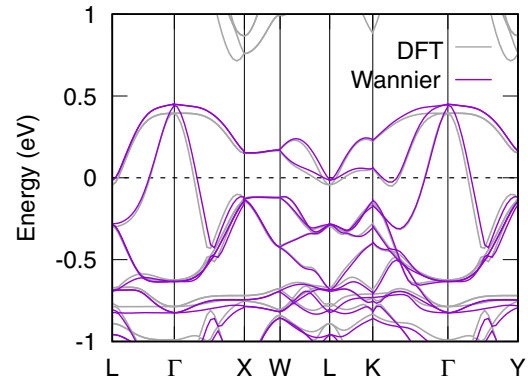

FIG. 7. Full DFT (gray) and Wannier interpolated (violet) band structures in the majority spin channel without spin-orbit coupling.

2. Tight-binding Wannier model

As mentioned in the main text, we have employed a 36-band tight-binding (TB) model, consisting of 12 Cr-t_{2g}-like and 24 Se-p-like Wannier orbitals in the majority spin channel, for a faithful representation of the nodal line features in our model. We note in passing that any trial to obtain TB models with fewer Wannier orbitals suffered from poor convergence issues that resulted in (i) imaginary hopping integrals even in the absence of SOC or (ii) disagreement in nodal line features between DFT and TB results. Because of the small number of minority spin components within $E_F \pm 0.5$ eV [see Fig. 1(b) in the main text], we expect that this spin-up Wannier TB model is the minimal model that captures physics induced by the nodal lines of CCS.

Figure 7 shows band structures in the majority spin channel, obtained within a full Kohn-Sham orbital basis (DFT) and minimal TB basis (Wannier). The interpolated Wannier bands are in good agreement with the full DFT bands of CCS around $E_F \pm 0.5$ eV, and aptly describe the key nodal-like band features on the X-W lines as shown in the figure.

Since the tight-binding (TB) Hamiltonian suffices to well describe the valence electrons within minimal basis set, here we build an *ab initio* TB model using a Wannier function. It is well known that most of relevant features of the topological materials originate from the relativistic effect. Hence, spin-orbit coupling is further added to the Hamiltonian. For t_{2g} (d_{yz}, d_{xz}, d_{xy}) orbitals and magnetization direction along [001] and [111], $H_{\text{SO}}^{t_{2g}}$ is

$$H_{\text{SO}}^{001} = \lambda_{\text{Cr}} \begin{bmatrix} 0 & -i & 0 \\ i & 0 & 0 \\ 0 & 0 & 0 \end{bmatrix}, \quad H_{\text{SO}}^{111} = \lambda_{\text{Cr}} \begin{bmatrix} 0 & -i & i \\ i & 0 & -i \\ -i & i & 0 \end{bmatrix}. \tag{A1}$$

Using the T-P equivalence relation [45], $l(t_{2g}) = -l(p)$, matrix elements of the spin-orbit Hamiltonian of the Se atom can be easily obtained from $H_{\text{SO}}^{t_{2g}}$. In the Wannier TB model, the strength of the spin-orbit coupling constants ($\lambda_{\text{Cr}} = 0.02$ eV and $\lambda_{\text{Se}} = 0.05$ eV) is chosen such that it produces roughly the same band splitting energies at the L point as those from DFT calculations.

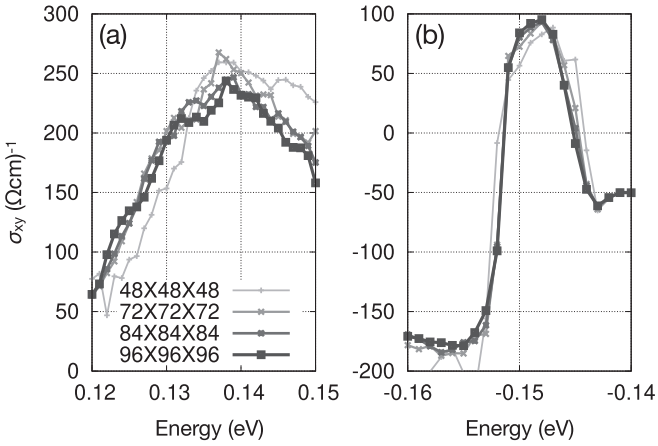

FIG. 8. Computed $\sigma_{xy}(E)$ with varying k-grid sampling in energy ranges of (a) $0.12 \leqslant E \leqslant 0.15$ and (b) $-0.16 \leqslant E \leqslant -0.14$ eV with respect to the Fermi level. $\mathbf{M}//[111]$ and nonzero $\lambda_{\mathrm{Cr,Se}}$ are included.

3. Chern number and anomalous Hall conductivity

To compute anomalous Hall conductivity, a numerically efficient approach, known as the Fukui-Hatsugai-Suzuki (FHS) method [39], is employed to calculate the Chern number in the discretized Brillouin zone. The FHS method computes the Berry curvature threading a k plaquette defined by 4 nearest-neighboring k points via the following formula,

$$\Omega_{\alpha\beta}(\mathbf{k}) = \frac{1}{2\pi i}\ln[U_\alpha(\mathbf{k})U_\beta(\mathbf{k}+\hat{k}_\alpha)U_\alpha(\mathbf{k}+\hat{k}_\beta)^{-1}U_\beta(\mathbf{k})^{-1}],$$

where the link matrix $U_\alpha(\mathbf{k})$ is defined as

$$U_\alpha(\mathbf{k}) \equiv \frac{\det\psi^\dagger(\mathbf{k})\psi(\mathbf{k}+\hat{k}_\alpha)}{|\det\psi^\dagger(\mathbf{k})\psi(\mathbf{k}+\hat{k}_\alpha)|}.$$

Here $\alpha, \beta = x, y, z$ are indices for Cartesian coordinates, $\hat{k}_\alpha$ are unit vectors in the discretized k space along the α direction, and $\psi(\mathbf{k})$ is the vector of occupied states at $\mathbf{k}$.

In metallic systems, the number of occupied bands can change as one crosses a Fermi surface in the k space. Then the size of the link matrix $U_\alpha(\mathbf{k})$ may not be well defined. To circumvent this issue and apply the FHS method in metallic systems, we introduced a mixing scheme to the original formulation. When the k plaquette from which a $\Omega_{\alpha\beta}(\mathbf{k})$ is computed intersects with a Fermi surface, then some of the vertices have a different number of occupied bands compared to others. If the k plaquette is small enough, there should be vertices with either N or $N+1$ occupied bands only. In such case we compute two $\Omega^{N,N+1}_{\alpha\beta}(\mathbf{k})$, one with N-occupied bands, another with $N+1$ bands. Then we take an average of $\Omega^{N}_{\alpha\beta}(\mathbf{k})$ and $\Omega^{N+1}_{\alpha\beta}(\mathbf{k})$ to obtain the final $\Omega_{\alpha\beta}(\mathbf{k})$.

To check the validity of this trick we did a convergence test of our AHC results as a function of k sampling. Figure 8 presents the result of the convergence test in the vicinity of the nodal-line-induced peak of AHC close to the Fermi level, which shows a reasonable convergence at $96 \times 96 \times 96$. In addition, the Berry curvature on a side face of the Brillouin zone X-W plane is calculated with the choice of a 200×200 k grid.

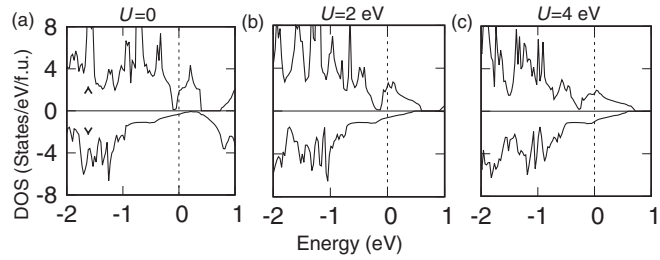

FIG. 9. Total density of states of CCS within (a) LDA and (b), (c) LDA+U, with $U = 2$, 4 eV demonstrate the effect of U on the electronic structure.

4. Dynamical mean-field theory

A combined density functional plus embedded dynamical mean-field theory (DMFT), as implemented in the Rutgers EDMFTF code [41,42], is further used to study the effect of dynamical electron correlation on the nodal line in the band structure. The LDA exchange-correlation functional, which provided a more consistent result with the experimental observation, is further chosen to combine with the DMFT. A primitive Brillouin zone is sampled with a $12 \times 12 \times 12$ mesh grid. $RK_{\max}$ is set to 7. The continuous-time quantum Monte Carlo method is employed to solve the quantum impurity problem in the correlated d-orbital subspaces of Cu and Cr. For each run, 2×10^8 Monte Carlo steps are carried out. The bath temperature is set to 116 K. A simplified Ising-type density-density Coulomb interaction is used. The hybridization window is taken to be -10 to $+10$ eV with respect to Fermi energy. For charge self-consistent DMFT calculation, the on-site Coulomb repulsion and Hund's coupling parameters are set to $U = 10$ and $J = 1$ eV for both Cu and Cr d orbitals.

APPENDIX B: EFFECT OF STATIC ELECTRON CORRELATIONS

In general, for studies of materials having partially filled d shells, often it is necessary to incorporate the on-site Coulomb repulsion parameter U in order to accurately calculate the electronic structure. Figure 9 shows how the inclusion of the U parameter affects the ground states of $CuCr_2Se_4$ within the mean-field-like DFT+U formalism. In the absence of U, states close to the Fermi level are predominantly occupied by hybridized Cr-t_{2g}–Se-p states in the majority spin channel, while they are almost empty in the minority spin channel. This nearly half-metallic picture is consistent with the earlier experimental observation [30]. When U is introduced to the d orbitals, the density of states of the minority spin channel is gradually enhanced and it becomes comparable to that of the majority spin at the Fermi level when $U = 4$ eV at Cr. We conclude that in the present case, the effects of the DFT+U correction drive the system away from the half-metallic phase, so that pure LDA seems to yield better agreement with the experimental observation.

Figure 10 summarizes the effect of the Hubbard U ($= 2$ eV) on the electronic band structure. In the main text, it has been shown that in the LDA band structure, upper nodal line lies in the electron-doped region which generates

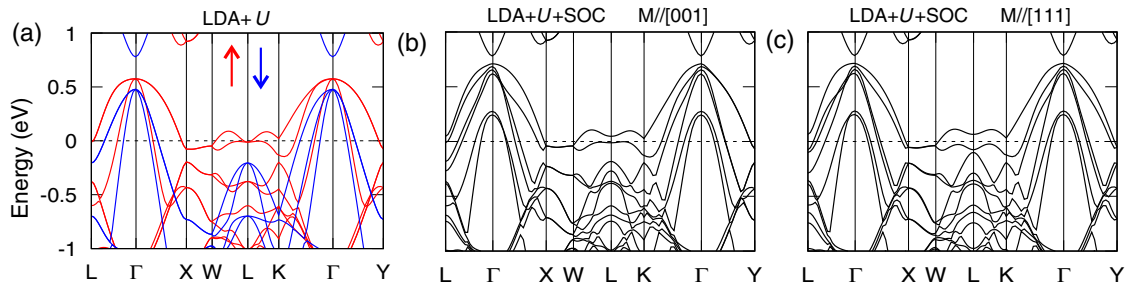

FIG. 10. Band structure of CCS demonstrates the effect of Hubbard U (= 2 eV) and spin-orbit coupling on the electronic structure. (a) An inclusion of U parameter pushes nodal line below Fermi level. (b), (c) SOC splits the band at L point.

a large anomalous Hall response upon electron doping. This observation is also consistent with experimental studies [23]. However, the band structure within DFT+U shows the opposite trend; the nodal lines, which were located just above the Fermi level in the absence of U, are pushed down in energy below the Fermi level in presence of U. Because the sign-changing behavior of the anomalous Hall response upon electron doping is likely relevant to the nodal lines, we suspect that application of the DFT+U method is detrimental to the study of this compound.

[1] M. J. Gilbert, Topological electronics, Commun. Phys. **4**, 70 (2021).

[2] Y. Fan and K. L. Wang, Spintronics based on topological insulators, SPIN **06**, 1640001 (2016).

[3] C.-Z. Chang, W. Zhao, D. Y. Kim, P. Wei, J. K. Jain, C. Liu, M. H. W. Chan, and J. S. Moodera, Zero-Field Dissipationless Chiral Edge Transport and the Nature of Dissipation in the Quantum Anomalous Hall State, Phys. Rev. Lett. **115**, 057206 (2015).

[4] S. Murakami, N. Nagaosa, and S.-C. Zhang, Dissipationless quantum spin current at room temperature, Science **301**, 1348 (2003).

[5] D. Culcer, A. C. Keser, Y. Li, and G. Tkachov, Transport in two-dimensional topological materials: Recent developments in experiment and theory, 2D Mater. **7**, 022007 (2020).

[6] K. He, Y. Wang, and Q.-K. Xue, Topological materials: Quantum anomalous Hall system, Annu. Rev. Condens. Matter Phys. **9**, 329 (2018).

[7] Y. Tokura, K. Yasuda, and A. Tsukazaki, Magnetic topological insulators, Nat. Rev. Phys. **1**, 126 (2019).

[8] N. Nagaosa, J. Sinova, S. Onoda, A. H. MacDonald, and N. P. Ong, Anomalous Hall effect, Rev. Mod. Phys. **82**, 1539 (2010).

[9] M. Z. Hasan and C. L. Kane, Colloquium: Topological insulators, Rev. Mod. Phys. **82**, 3045 (2010).

[10] X. Wan, A. M. Turner, A. Vishwanath, and S. Y. Savrasov, Topological semimetal and Fermi-arc surface states in the electronic structure of pyrochlore iridates, Phys. Rev. B **83**, 205101 (2011).

[11] K.-Y. Yang, Y.-M. Lu, and Y. Ran, Quantum Hall effects in a Weyl semimetal: Possible application in pyrochlore iridates, Phys. Rev. B **84**, 075129 (2011).

[12] R. Yu, W. Zhang, H.-J. Zhang, S.-C. Zhang, X. Dai, and Z. Fang, Quantized anomalous Hall effect in magnetic topological insulators, Science **329**, 61 (2010).

[13] C.-Z. Chang, J. Zhang, X. Feng, J. Shen, Z. Zhang, M. Guo, K. Li, Y. Ou, P. Wei, L.-L. Wang, Z.-Q. Ji, Y. Feng, S. Ji, X. Chen, J. Jia, X. Dai, Z. Fang, S.-C. Zhang, K. He, Y. Wang *et al.*, Experimental observation of the quantum anomalous Hall effect in a magnetic topological insulator, Science **340**, 167 (2013).

[14] C.-Z. Chang, W. Zhao, D. Y. Kim, H. Zhang, B. A. Assaf, D. Heiman, S.-C. Zhang, C. Liu, M. H. W. Chan, and J. S. Moodera, High-precision realization of robust quantum anomalous Hall state in a hard ferromagnetic topological insulator, Nat. Mater. **14**, 473 (2015).

[15] G. Xu, H. Weng, Z. Wang, X. Dai, and Z. Fang, Chern Semimetal and the Quantized Anomalous Hall Effect in $HgCr_2Se_4$, Phys. Rev. Lett. **107**, 186806 (2011).

[16] Z. Wang, M. G. Vergniory, S. Kushwaha, M. Hirschberger, E. V. Chulkov, A. Ernst, N. P. Ong, R. J. Cava, and B. A. Bernevig, Time-Reversal-Breaking Weyl Fermions in Magnetic Heusler Alloys, Phys. Rev. Lett. **117**, 236401 (2016).

[17] S. Nakatsuji, N. Kiyohara, and T. Higo, Large anomalous Hall effect in a non-collinear antiferromagnet at room temperature, Nature (London) **527**, 212 (2015).

[18] K. Kim, J. Seo, E. Lee, K.-T. Ko, B. S. Kim, B. G. Jang, J. M. Ok, J. Lee, Y. J. Jo, W. Kang, J. H. Shim, C. Kim, H. W. Yeom, B. I. Min, B.-J. Yang, and J. S. Kim, Large anomalous Hall current induced by topological nodal lines in a ferromagnetic van der Waals semimetal, Nat. Mater. **17**, 794 (2018).

[19] B.-J. Yang, T. A. Bojesen, T. Morimoto, and A. Furusaki, Topological semimetals protected by off-centered symmetries in nonsymmorphic crystals, Phys. Rev. B **95**, 075135 (2017).

[20] Y. Sun, Y. Zhang, C.-X. Liu, C. Felser, and B. Yan, Dirac nodal lines and induced spin Hall effect in metallic rutile oxides, Phys. Rev. B **95**, 235104 (2017).

[21] S.-Y. Yang, H. Yang, E. Derunova, S. S. P. Parkin, B. Yan, and M. N. Ali, Symmetry demanded topological nodal-line materials, Adv. Phys.: X **3**, 1414631 (2018).

[22] W.-L. Lee, S. Watauchi, V. L. Miller, R. J. Cava, and N. P. Ong, Dissipationless anomalous Hall current in the ferromagnetic spinel $CuCr_2Se_{4-x}Br_x$, Science **303**, 1647 (2004).

[23] W.-L. Lee, S. Watauchi, V. L. Miller, R. J. Cava, and N. P. Ong, Anomalous Hall Heat Current and Nernst Effect in

the $CuCr_2Se_{4-x}Br_x$ Ferromagnet, Phys. Rev. Lett. **93**, 226601 (2004).

[24] D. Xiao, Y. Yao, Z. Fang, and Q. Niu, Berry-Phase Effect in Anomalous Thermoelectric Transport, Phys. Rev. Lett. **97**, 026603 (2006).

[25] Y. Yao, Y. Liang, D. Xiao, Q. Niu, S.-Q. Shen, X. Dai, and Z. Fang, Theoretical evidence of the Berry-phase mechanism in anomalous Hall transport: First-principles studies of $CuCr_2Se_{4-x}Br_x$, Phys. Rev. B **75**, 020401(R) (2007).

[26] I. Nakatani, H. Nose, and K. Masumoto, Magnetic properties of $CuCr_2Se_4$ single crystals, J. Phys. Chem. Solids **39**, 743 (1978).

[27] G. Kresse and J. Furthmüller, Efficient iterative schemes for *ab initio* total-energy calculations using a plane-wave basis set, Phys. Rev. B **54**, 11169 (1996).

[28] I. Souza, N. Marzari, and D. Vanderbilt, Maximally localized Wannier functions for entangled energy bands, Phys. Rev. B **65**, 035109 (2001).

[29] G. Pizzi, V. Vitale, R. Arita, S. Blëgel, F. Freimuth, G. Géranton, M. Gibertini, D. Gresch, C. Johnson, T. Koretsune, J. Ibañez-Azpiroz, H. Lee, J.-M. Lihm, D. Marchand, A. Marrazzo, Y. Mokrousov, J. I. Mustafa, Y. Nohara, Y. Nomura, L. Paulatto *et al.*, Wannier90 as a community code: New features and applications, J. Phys.: Condens. Matter **32**, 165902 (2020).

[30] A. Kimura, J. Matsuno, J. Okabayashi, A. Fujimori, T. Shishidou, E. Kulatov, and T. Kanomata, Soft x-ray magnetic circular dichroism study of the ferromagnetic spinel-type Cr chalcogenides, Phys. Rev. B **63**, 224420 (2001).

[31] B. Feng, R.-W. Zhang, Y. Feng, B. Fu, S. Wu, K. Miyamoto, S. He, L. Chen, K. Wu, K. Shimada, T. Okuda, and Y. Yao, Discovery of Weyl Nodal Lines in a Single-Layer Ferromagnet, Phys. Rev. Lett. **123**, 116401 (2019).

[32] Y. Kim, B. J. Wieder, C. L. Kane, and A. M. Rappe, Dirac Line Nodes in Inversion-Symmetric Crystals, Phys. Rev. Lett. **115**, 036806 (2015).

[33] K. Manna, L. Muechler, T.-H. Kao, R. Stinshoff, Y. Zhang, J. Gooth, N. Kumar, G. Kreiner, K. Koepernik, R. Car, J. Kübler, G. H. Fecher, C. Shekhar, Y. Sun, and C. Felser, From Colossal to Zero: Controlling the Anomalous Hall Effect in Magnetic Heusler Compounds via Berry Curvature Design, Phys. Rev. X **8**, 041045 (2018).

[34] J. Noky, Q. Xu, C. Felser, and Y. Sun, Large anomalous Hall and Nernst effects from nodal line symmetry breaking in Fe_2MnX (X = P, As, Sb), Phys. Rev. B **99**, 165117 (2019).

[35] P. Li, J. Koo, W. Ning, J. Li, L. Miao, L. Min, Y. Zhu, Y. Wang, N. Alem, C.-X. Liu, Z. Mao, and B. Yan, Giant room temperature anomalous Hall effect and tunable topology in a ferromagnetic topological semimetal Co_2MnAl, Nat. Commun. **11**, 3476 (2020).

[36] S. Minami, F. Ishii, M. Hirayama, T. Nomoto, T. Koretsune, and R. Arita, Enhancement of the transverse thermoelectric conductivity originating from stationary points in nodal lines, Phys. Rev. B **102**, 205128 (2020).

[37] N. Marzari and D. Vanderbilt, Maximally localized generalized Wannier functions for composite energy bands, Phys. Rev. B **56**, 12847 (1997).

[38] H. Weng, T. Ozaki, and K. Terakura, Revisiting magnetic coupling in transition-metal-benzene complexes with maximally localized Wannier functions, Phys. Rev. B **79**, 235118 (2009).

[39] T. Fukui, Y. Hatsugai, and H. Suzuki, Chern numbers in discretized Brillouin zone: Efficient method of computing (spin) Hall conductances, J. Phys. Soc. Jpn. **74**, 1674 (2005).

[40] S. L. Dudarev, G. A. Botton, S. Y. Savrasov, C. J. Humphreys, and A. P. Sutton, Electron-energy-loss spectra and the structural stability of nickel oxide: An LSDA+U study, Phys. Rev. B **57**, 1505 (1998).

[41] K. Haule, C.-H. Yee, and K. Kim, Dynamical mean-field theory within the full-potential methods: Electronic structure of $CeIrIn_5$, $CeCoIn_5$, and $CeRhIn_5$, Phys. Rev. B **81**, 195107 (2010).

[42] K. Haule, Structural predictions for correlated electron materials using the functional dynamical mean field theory approach, J. Phys. Soc. Jpn. **87**, 041005 (2018).

[43] A. Deb, M. Itou, V. Tsurkan, and Y. Sakurai, Effect of substitution of Cl and Br for Se in the ferromagnetic spinel $CuCr_2Se_4$: A magnetic Compton profile study, Phys. Rev. B **75**, 024413 (2007).

[44] D. M. Ceperley and B. J. Alder, Ground State of the Electron Gas by a Stochastic Method, Phys. Rev. Lett. **45**, 566 (1980).

[45] S. Sugano, Y. Tanabe, and H. Kamimura, *Multiplets of Transition-Metal Ions in Crystals* (Academic, New York, 1970).